Vortex Model and Blade Span Influence on Orthogonal Blade-Vortex Interaction Noise

Paul Zehner, Fabrice Falissard, Xavier Gloerfelt

Vortex Model and Blade Span Infuence on Orthogonal Blade/Vortex Interaction Noise

Paul Zehner*
DAAA, ONERA, Université Paris Saclay,
F-92322 Châtillon, France

Fabrice Falissard†
DAAA, ONERA, Université Paris Saclay,
F-92120 Meudon, France

Xavier Gloerfelt‡
Arts et Métiers ParisTech, Dynfluid laboratory,
F-75013 Paris, France

The influence of vortex impingement location, on the aerodynamic and acoustic response of a rotating blade during an orthogonal interaction, is studied by means of computational fluid dynamics. The objective is to identify and quantify precisely the noise reduction achieved by reducing the blade span. The Batchelor vortex model is primarily considered as it accounts for the axial velocity deficit observed in the core of realistic tip vortices. Separated simulations were also carried out for a Lamb-Oseen vortex and a purely axial velocity deficit to highlight and quantify the influence of the vortex velocity components on the interaction as well as to balance design optimizations performed relying on methods not able to model viscous effects. Analysis of the blade aerodynamic and acoustic responses show that the magnitude of the thrust fluctuation and radiated noise are always higher for a Batchelor vortex than for a Lamb-Oseen vortex when the vortex core impinges below the blade tip. For both vortex models, the thrust fluctuation and radiated noise reach their peak for an interaction close to the blade tip. They decrease slowly as the vortex impingement moves inward the blade and decrease strongly as the vortex passes above the tip. Finally, the noise directivity pattern is dipolar for interaction close to or above the blade tip and becomes more and more quadrupolar as the radius of interaction moves toward the blade root.

Nomenclature

BPF	blade passing frequency, Hz	r_c	vortex core radius, m
C	blade chord, m	SWL	sound power level dB
C_p	pressure coefficient	T	thrust, N
C_T	thrust coefficient	v_a	vortex axial velocity, m s^{-1}
M_h	blade helical Mach number	v_{Hel}	helical velocity, m s^{-1}
M_0	blade tip rotational Mach number	v_θ	vortex tangential velocity, m s^{-1}
n	angular frequency, Hz	v_∞	upstream flow velocity, m s^{-1}
p	pressure, Pa	v_u^*	dimensionless upwash velocity
R_{Int}	blade/vortex interaction radius m	β	angle of attack, deg
R^*_{Int}	relative interaction radius	Ω	blade angular velocity rad s^{-1}
R_0	reference blade tip radius, m	$\bullet_\infty$	upstream value
R_t	blade tip radius, m	$\widetilde{\bullet}$	fluctuating value
R^*_t	relative blade tip radius		

*PhD student during this work, now postdoctoral researcher at JAXA, paul.zehner@alumni.enseeiht.fr.
†Research Scientist, fabrice.falissard@onera.fr, corresponding author.
‡Professor, xavier.gloerfelt@ensam.eu.

I. Introduction

Orthogonal blade/vortex interactions (OBVI) occur on single propellers in pusher configuration or on aft rotors of contra-rotating open-rotors (CROR) that operate in the wake of a fixed or rotating lifting surface. This wake, consisting of a velocity deficit and of vortices generated at the tip or root, gives rise to impulsive thrust and torque fluctuations on the propeller, increasing significantly vibrations and noise radiation. These phenomena can be partially mitigated by placing adequately the side-edges of the control surfaces upstream to a single propeller or by reducing the radius of the aft rotor on CRORs [1]. This is usually done in the early stages of the design process using preliminary design methods unable to handle the complexity of OBVI.

In the past, OBVI has been studied thoroughly within the helicopter field with a focus on main rotor/tail rotor interactions [2]. Analyses were carried out by means of dedicated experiments [3–10], analytical modeling [11, 12] and numerical computations [7, 13–19]. These studies came to the conclusion that OBVI is complex and exhibit various regimes depending on several non-dimensional parameters such as: the ratio of the vortex advection speed and vortex maximum tangential velocity, the ratio of the blade thickness and vortex core radius, the ratio of the vortex axial velocity deficit or excess and vortex maximum tangential velocity. Yet, most of the computations performed in the studies cited above were carried out considering untwisted rectilinear blades with translation motion, which is quite different to the blade/vortex interaction occurring on propellers and open rotors. In fact, the blade rotation, the rotor advance ratio, and the location of the interaction on the blade influence strongly the blade aeroacoustic response to the interaction. These parameters have started to be accounted for in recent studies launched to better understand and characterize OBVI [20–25] in the context of open rotors and to improve the reliability of fast prediction methods [26–28].

Roger et al. [26] showed by analytical means that for a Lamb-Oseen vortex interacting with a finite blade, the radiated noise is maximum when the vortex impinges exactly at the blade tip. The noise decreases as the impingement occurs closer to the blade root, and decreases even sharper as it occurs above the blade tip. Yang et al. [24, 25] simulated the interaction of a propeller with a Batchelor vortex. They found that blade torque fluctuation increases as the interaction occurs closer to the blade tip and deduced that maximum torque fluctuation is obtained for an impingement at the blade tip. Zehner et al. [23] focused on the relative influence of vortex axial and tangential velocities on the aerodynamic and acoustic response of the blade during the interaction. They showed that the vortex tangential velocity is responsible for the low-frequency content of the thrust fluctuation and noise radiation, whereas the axial velocity deficit in the vortex core accounts for the high-frequency content, with some constructive interference mechanism in between.

The present paper investigates the influence of the vortex impingement location on the blade aerodynamic and acoustic response to the interaction. It extends previous results and analyses [29], with the objective to identify and quantify precisely the noise reduction achieved by reducing the blade span in order to avoid the vortex core during the interaction. The dimensionless parameters characterizing the vortex response [2] are the same as in Ref. [23], resulting in a subcritical interaction in the weak-vortex regime where the cutting of the vortex by the blade does not alter significantly the vortex structure. For this type of interaction, Liu and Marshall [16] have demonstrated that the physical mechanisms governing the cutting process are mostly inviscid, and that the flow physics is not particularly sensitive to Reynolds number. The governing equations solved for the current study are thus the unsteady Euler equations in the compressible regime, that have proven to capture the main physical phenomena of blade/vortex interaction with respect to blade aerodynamic and aeroacoustic responses [30].

To be as representative as possible, this study considers a Batchelor vortex model to account for the axial velocity deficit observed in the core of realistic tip vortices. However, aerodynamic preliminary design studies and optimizations are often carried out relying on fast prediction methods, for instance lifting line or panel methods, that cannot account for viscous features and results in tip vortices consisting only in tangential velocity fields. Simulations are thus also performed considering separately a Lamb-Oseen vortex and a purely axial velocity deficit to highlight and quantify the influence of the vortex velocity components on the interaction as well as to balance the results of design optimization performed relying on such methods.

The paper is organized as follows. Section II presents the blade geometries, vortex characteristics and numerical setup of the OBVI simulations carried out for this study. The results are presented and analyzed in section III, first from an aerodynamic viewpoint, and then from an aeroacoustic perspective.

II. Setup of the numerical experiment

The numerical setup is derived from the one used in a previous study to analyze the aeroacoustic response of a rotating blade interacting with a Batchelor vortex for an impingement located at 90% of the blade span [23]. It consists in a single blade of external radius $R_0 = 1\,\mathrm{m}$, of inner radius $R_{\mathrm{root}} = 0.2\,\mathrm{m}$, with NACA 0002 airfoil section of chord $C = 0.2\,\mathrm{m}$, rotating with a tip Mach number $M_0 = 0.65$ within a coaxial flow of upstream Mach number $M_\infty = 0.25$, as sketched in Fig. 1. The vortex model considered in this study is a Batchelor vortex [31], with core radius $r_c = 2.5 \times 10^{-2} R_0$. The tangential velocity magnitude is set to one quarter of the blade tip helical velocity, $v_\theta^{\max} = v_{\mathrm{Hel_{Tip}}}/4$ with $v_{\mathrm{Hel_{Tip}}} = (M_\infty^2 + M_0^2)^{1/2}/c_0$, and c_0 the sound speed. The magnitude of the Gaussian axial velocity deficit in the core $v_a^{\max}$ is taken equal to $v_\theta^{\max}$. The infinite upstream flow in the reference frame attached to the vortex center is thus given by:

$$v_\theta = v_\theta^{\max}(1 - e^{-\alpha^2\bar{r}^2})/(\bar{r}(1 - e^{-\alpha^2})) \quad (1)$$

$$v_x = v_\infty - v_a^{\max} e^{-\alpha^2\bar{r}^2} \quad (2)$$

with $\alpha \simeq 1.121$ so that the maximum tangential velocity is reached for $\bar{r} = 1$. Density and pressure fields are calculated by integrating the radial equilibrium equation with an homentropic hypothesis. In order to better quantify the contribution to the interaction of the vortex tangential and axial velocity components, simulations have also been carried out considering separately a Lamb-Oseen vortex [32, 33], with tangential flow field given by eqn (1), and with a purely Gaussian axial velocity deficit of eqn (2).

The three dimensional unsteady compressible Euler simulations are computed using a near-body/off-body meshing strategy [34, 35], with a curvilinear blade mesh rotating within an octree of Cartesian meshes. Contrarily to viscosity, compressibility cannot be neglected *a priori* due to the relative high helical Mach number of the blade section interacting with the vortex core. Actually, depending on the vortex strength and blade thickness, flow acceleration at the blade leading edge could lead to the formation of supersonic pockets possibly resulting in the creation of vorticity or vortices due to the loss of colinearity of the density and pressure gradient (baroclinic term of the vorticity equation) through curved shocks [30].

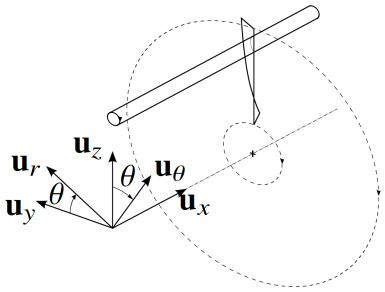

Fig. 1 Scheme of the blade/vortex interaction.

The spatial discretization schemes are respectively third-order and fifth-order accurate [36, 37] on the near-body curvilinear meshes and background Cartesian meshes. The time integration is implicit and second-order accurate. The computational fluid dynamics (CFD) is coupled with an aeroacoustic integral method to compute the noise generated by the interaction. The Ffowcs-Williams and Hawkings equation [38] is solved in its rotating solid surface formulation [39] to compute the noise radiated on a sphere of radius $20R_0$. The Fourier analysis of the time acoustic signal is performed for 100 harmonics of the Blade Passing Frequency ($BPF \approx 35.17\,\mathrm{Hz}$). More details about the computational setup and its accuracy can be found in Ref. [23].

In order to change the interaction location, only the blade span has been modified, all other parameters have been kept constant. For all cases the radius at which the vortex impinges on the blade is thus $R_{\mathrm{Int}} = 0.9R_0$. The simulations have been run for seven blades with relative tip radii, defined as $R^*_{\mathrm{Tip}} = R_{\mathrm{Tip}}/R_0$, ranging from 0.818 to 1.125. These values have been chosen so that the relative interaction radius, defined as $R^*_{\mathrm{Int}} = R_{\mathrm{Int}}/R_{\mathrm{Tip}}$, varies linearly between 0.8 and 1.1, see Tab. 1. The vortex core impinges at the blade tip for $R^*_{\mathrm{Int}} = 1$, above for $R^*_{\mathrm{Int}} > 1$, and below for $R^*_{\mathrm{Int}} < 1$. The different blade geometries and surfaces affected by the blade/vortex interaction are represented in Fig. 2.

Table 1 Relative blade tip and blade/vortex interaction radii.

R^*_{Tip}	0.818	0.857	0.9	0.947	1	1.059	1.125
R^*_{Int}	1.1	1.05	1	0.95	0.9	0.85	0.8

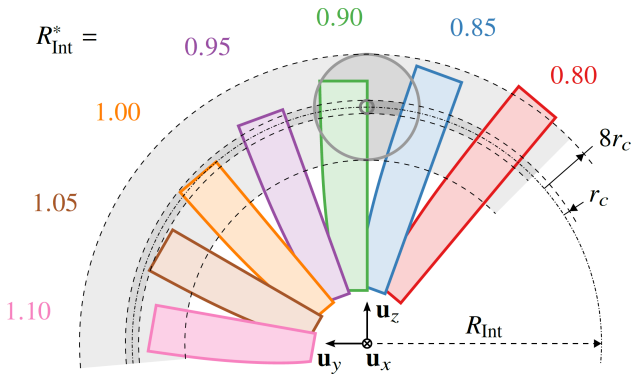

Fig. 2 Area of blade/vortex interaction depending on the blade span.

For each blade geometry, three simulations were performed, one with a Batchelor vortex (tangential vortex with axial flow), one with a Lamb-Oseen vortex, and one with a Gaussian axial velocity deficit. Note that an extra computation for the smaller blade was done without vortex to quantify the numerical noise of the setup.

III. Results and discussions

A. Blade aerodynamic response to the interaction

For an OBVI between a blade in translation motion and a vortex without axial velocity, the flow exhibits a symmetry between the upper and lower sides of the blade and no lift is created during the interaction. This is not the case anymore when a rotation motion is added to the blade. In this configuration, any flow disturbance will create an unsteady thrust component, positive or negative, depending on the modification of the velocity triangle at each radial station. The velocity triangles accounting for the Batchelor and Lamb-Oseen vortices, and axial velocity deficit are compared to the velocity triangles without perturbation in Fig. 3 for blade radial stations corresponding to the vortex center, and the vortex center plus or minus the vortex radius.

In case of an interaction with a Lamb-Oseen vortex exhibiting the same direction of rotation as the blade, the summation of the mean flow and vortex velocity components increases the relative velocity seen by the blade at $R = R_{\text{Int}} - r_c$, and generates a positive incidence. At this radial station, the Lamb-Oseen vortex interaction results in a local upwash and a positive thrust fluctuation. At $R = R_{\text{Int}} + r_c$, we observe a decrease of the relative velocity as well as a negative incidence, resulting in a local downwash and a negative thrust fluctuation at this radial station during the interaction. Note that since the velocity is zero in the vortex core, the Lamb-Oseen vortex does not alter the relative velocity at $R = R_{\text{Int}}$.

In case of an interaction with a purely axial velocity deficit, we observe in Fig. 3 a decrease of the norm of the relative velocity seen by the blade and a positive incidence for the three radial stations. The interaction with an axial velocity deficit leads to an upwash around the radial station $R = R_{\text{Int}}$, and thus a positive thrust fluctuation. The maximum incidence is obtained at $R = R_{\text{Int}}$.

Finally, for an interaction with a Bachelor vortex, whose velocity field is the summation of the Lamb-Oseen vortex and the axial velocity deficit, we observe an increase of the velocity norm and a strong positive incidence at radial station $R = R_{\text{Int}} - r_c$, and a decrease of the velocity norm and a lesser negative incidence at radial station $R = R_{\text{Int}} + r_c$. The behavior at $R = R_{\text{Int}}$ is similar to the one observed for the axial velocity deficit. The Batchelor vortex generates an upwash, respectively a downwash, on the blade span below, respectively above, the interaction radius. Consequently, when the vortex core is chopped by the blade, the latter experiences a positive thrust fluctuation from the root and approximately up to the interaction radius and a negative thrust fluctuation on the upper part and up to the blade tip. This phenomenon can also be observed on the unsteady component of the pressure coefficient at the blade leading edge, plotted in Fig. 4, where the areas colored in red highlight the displacement of the stagnation point along the blade span during the interaction.

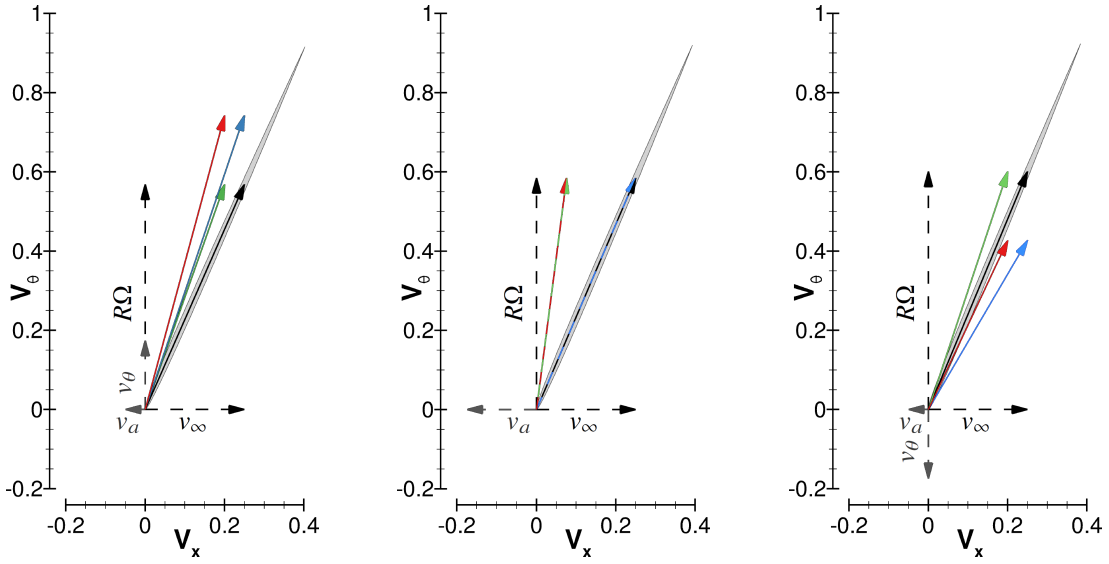

(a) $R = R_{\text{Int}} - r_c$ **(b)** $R = R_{\text{Int}}$ **(c)** $R = R_{\text{Int}} + r_c$

Fig. 3 Velocity triangle modifications at blade azimuth zero and at different blade radii depending on the velocity perturbations added to the meanflow. No perturbation (——), Batchelor vortex (——), Lamb-Oseen vortex (——), axial velocity deficit (——).

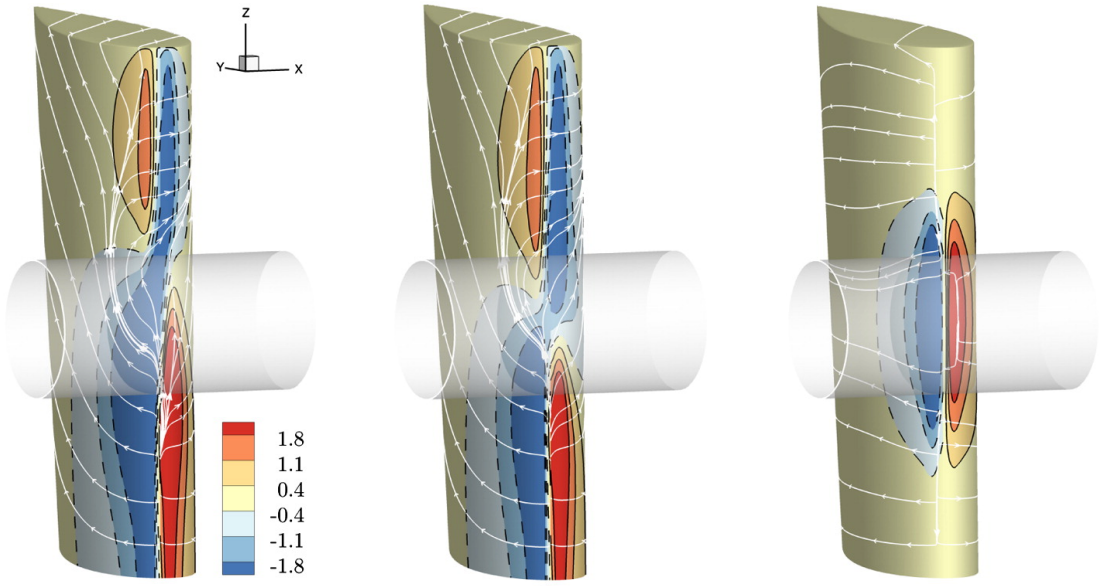

(a) Batchelor vortex **(b) Lamb-Oseen vortex** **(c) Axial velocity deficit**

Fig. 4 Pressure coefficient fluctuation and streamlines on the blade leading edge at azimuth 0 deg for the interaction at $R^*_{\text{Tip}} = 1$ (i.e. $R^*_{\text{Int}} = 0.9$) with different flow perturbations. Blade thickness enlarged for visualisation.

Let us introduce the relative upwash velocity experienced by the blade at the azimuth of interaction, defined by $v^*_{\text{upwash}} = v_{\text{upwash}}/v_{\text{Hel}}$, where v_{upwash} is the projection of the instantaneous velocity on the direction normal to the blade chord, and v_{Hel} is the kinematic helical velocity, *i.e.* the colored arrows in Fig. 3. The formula giving v^*_{upwash} was derived in Ref. [23] from the vortex tangential and axial velocities, blade kinematics, and blade geometry. It is plotted in Fig. 5 as a function of the non-dimensional interaction radius R^*_{Int}. For a Batchelor vortex having tangential and axial velocity components of same magnitude, this upwash changes of sign slightly above the vortex center, resulting in a downwash on the external part of the blade. For a Lamb-Oseen vortex, this sign change occurs exactly at the vortex center while it is always positive for a purely axial velocity deficit. For the different blade spans considered in this study, it is thus expected that the maximum thrust fluctuation due to the OBVI will be reached for a vortex impingement radius corresponding to the sign change of the upwash.

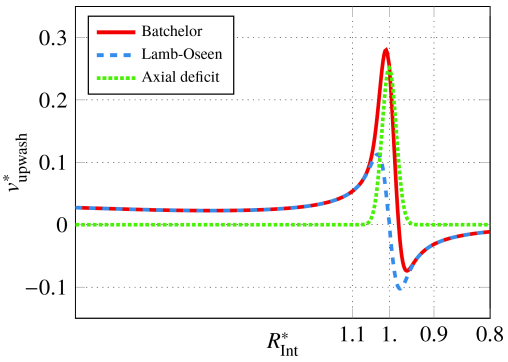

Fig. 5 Relative upwash velocity induced by the vortex in the frame attached to the blade section at the azimuth of interaction.

The unsteady component of the blade thrust coefficient [40], based on the reference blade radius and defined as $C_T^{R_0} = T/(16\rho_\infty n^2 R_0^4)$ with T the thrust, ρ the density, and n the blade angular frequency, is plotted in Fig. 6 for azimuth angles around the interaction. Only four cases are displayed to enhance readability. The interaction is clearly visible close to 360° and the thrust fluctuation has a larger magnitude and a steeper shape at its maximum for the Batchelor vortex than for the Lamb-Oseen vortex. This is due to the contribution of the axial velocity deficit in the vortex core that results in an impulsive and localized thrust fluctuation that adds itself to the thrust fluctuation due to the tangential velocity component.

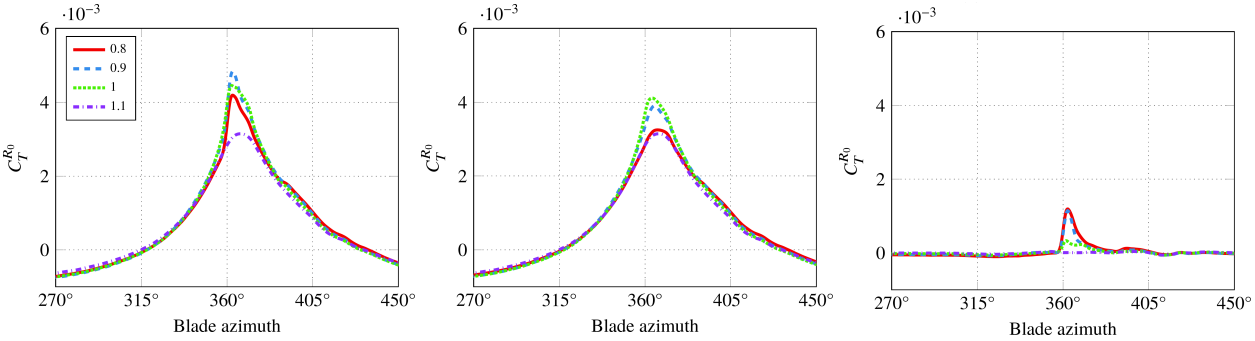

(a) Batchelor vortex. **(b) Lamb-Oseen vortex.** **(c) Axial deficit.**

Fig. 6 Evolution of thrust coefficient during orthogonal blade/vortex interaction for different values of R^*_{Int}.

The highest thrust fluctuations are observed for interaction radii close to the blade tip, with a significant decrease when the vortex core impinges lower on the blade or passes above the blade tip. The maximal value of the thrust coefficient is plotted in Fig. 7 for all relative interaction radii of Tab. 1. For interactions with a Lamb-Oseen vortex, the magnitude of thrust fluctuation increases progressively with the interaction radius, reaching a maximum exactly at the blade tip. The peak of the thrust fluctuation is always greater for the Batchelor vortex with a similar rise as the blade tip is approached and a rapid fall when the vortex core passes above the blade tip. The magnitude is then almost equal for the two vortex models. The maximum value for the Batchelor vortex is reached for an interaction radius slightly before the tip, for R^*_{Int} between 0.95 and 1.

For each vortex model, the highest thrust fluctuation is reached when the whole blade experiences a positive velocity upwash during the interaction. For the Lamb-Oseen vortex, this happens when the vortex core impinges at the blade tip. For the Batchelor vortex, the flow incidence variation β depending on the blade section, derived in Ref. [23], yields:

$$\beta = \arctan \frac{v_\infty - v_a(r - R_{\text{Int}})}{-r\Omega + v_\theta(r - R_{\text{Int}})} + \arctan \frac{v_\infty}{r\Omega} \qquad (3)$$

where v_∞ is the upstream flow velocity, and Ω is the angular speed. Looking back at Fig. 3, the incidence variation β is the angle between the relative velocities seen by a blade section with and without flow pertubation. Its value is plotted for both vortex models and the purely axial velocity deficit in Fig. 8. The curve corresponding to the Batchelor vortex with tangential and axial velocities of same magnitude becomes negative for a radius slightly higher than the vortex center. For our interaction parameters, equation (3) shows that β is positive for $r \leq 0.921$ and negative for $r \geq 0.921$, meaning that the blade aerodynamic response is maximum when the vortex core impacts just below the blade tip, for $R^*_{\text{Tip}} = 0.921$, *i.e.* $R^*_{\text{Int}} = 0.977$. This value is slightly below the one extrapolated by Yang et al. [25].

The pressure coefficient C_p on the blade suction side at azimuth 360° is displayed in Fig. 9 for four relative interaction radii. The aerodynamic response of the blade to the OBVI is mostly located around the blade leading edge, extending from the blade root to the blade tip. This large extension is due to the low decay of the potential velocity field of the vortex and means that OBVI cannot be fully avoided by cropping a blade. The change of sign of the pressure coefficient on the suction side is located very close to R_{Int} for the Lamb-Oseen vortex and is slightly shifted toward the blade tip for the Batchelor vortex in accordance with the variation of flow incidence displayed in Fig. 5. Finally it is noteworthy that the C_p distribution on all blades is very close to the one that would be obtained by truncating the blade with the largest span.

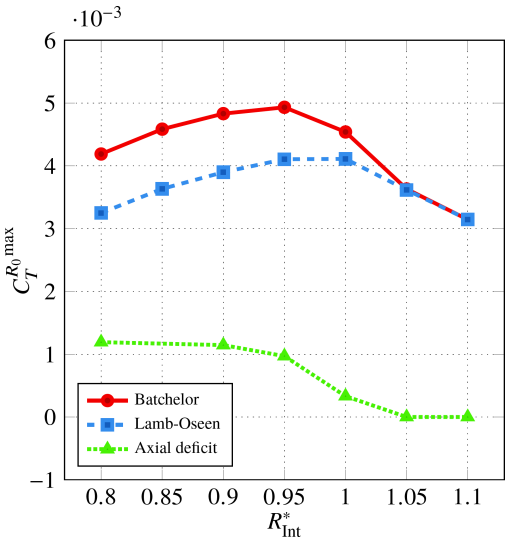

Fig. 7 Maximum value of thrust coefficient as a function of R^*_{Int}.

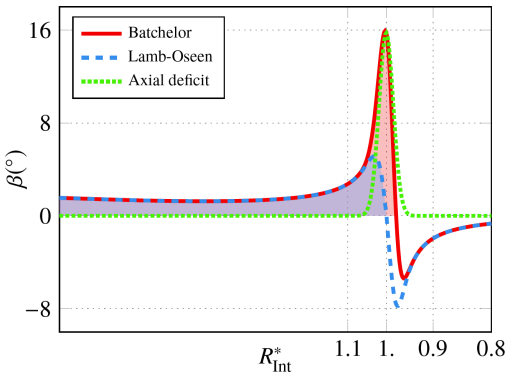

Fig. 8 Variation of flow incidence induced by the vortex in the frame attached to the blade section.

B. Blade acoustic response to the interaction

The noise radiated in the far-field by the OBVI has been computed on a sphere of radius $20R_0$. The acoustic signatures have been Fourier-transformed and integrated to compute the over all sound power level (OASWL), plotted in Fig. 10. The trend observed on the OASWL is very similar to the one already observed on the thrust fluctuation displayed in Fig. 7. For interactions with a Lamb-Oseen vortex, the OASWL increases progressively as the vortex core moves toward the blade tip and decreases with a stronger rate as the vortex core passes the blade tip. This behavior is coherent with the results obtained by Roger et al. [26] for this vortex model. For interactions with a Batchelor vortex, the OASWL increases also progressively as the vortex core moves toward the blade tip but the maximum is reached for R^*_{Int} between 0.95 and 1. Once the maximum is reached, the slope of the OASWL decreases drastically and for $R^*_{\text{Int}} \geq 1.05$, the levels become the same for the two vortex models since the axial velocity deficit within the vortex core does not impinge on the blade anymore. The contribution of the axial velocity deficit results in an increase of 4 dB for $R^*_{\text{Int}} \leq 0.95$ on the OASWL for the Batchelor vortex, and of 2 dB when the impact occurs at the blade tip.

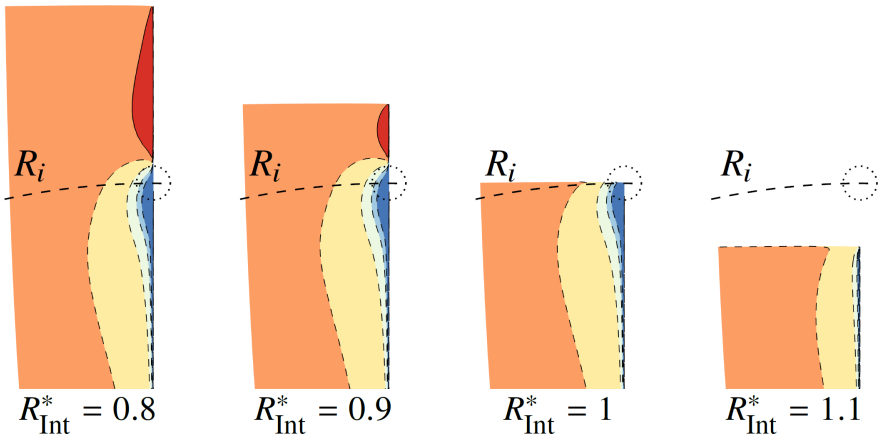

(a) Batchelor vortex.

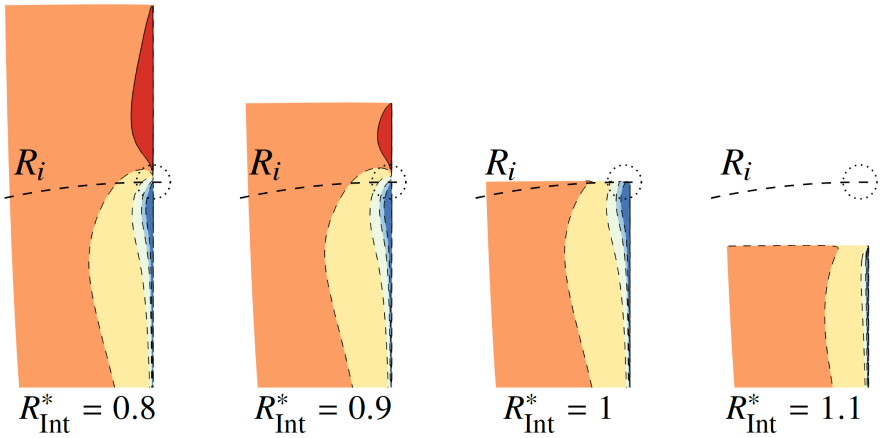

(b) Lamb-Oseen vortex.

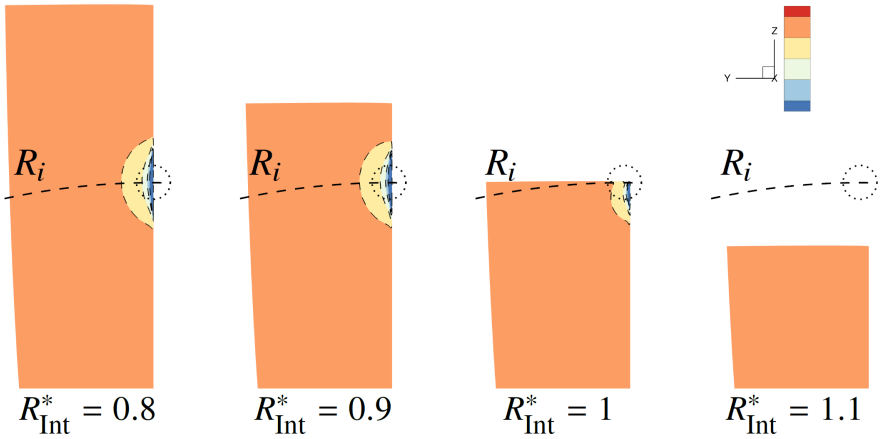

(c) Axial deficit.

Fig. 9 Pressure coefficient C_p on the blade suction side for different blade spans. Blade at azimuth 360°.

The sound power levels (SWLs) of the blade fundamental and its harmonics are plotted in Fig. 11 for a selection of blades, for the two vortex models and the axial velocity deficit. For the two blade-vortex interactions, the maxima are obtained for BPF = 2 and follow the trend observed for the OASWL, with highest levels for interactions near the blade tip. Consistently, SWLs are always higher for the interaction with the Batchelor vortex, with a significant contribution at high frequencies which is due to the axial component, as demonstrated in [23]. Since this supplementary contribution vanishes as the vortex passes above the tip, the curves are identical for both vortex models for $R^*_{\text{Int}} \geq 1.05$. For interactions with a Lamb-Oseen vortex, the SWLs decrease strongly and linearly up to a certain frequency after which the slope becomes less steep. This transition frequency varies with the radius of interaction on the blade. For interactions with a Batchelor vortex, the gentler slope of the spectra is due to the mid- and high-frequency contributions of the Gaussian velocity deficit in the vortex core [23] also plotted in Fig. 11. Consequently, the gap between the Batchelor and Lamb-Oseen interactions increases with the frequency, and its amplitude is directly linked to the magnitude of the velocity deficit.

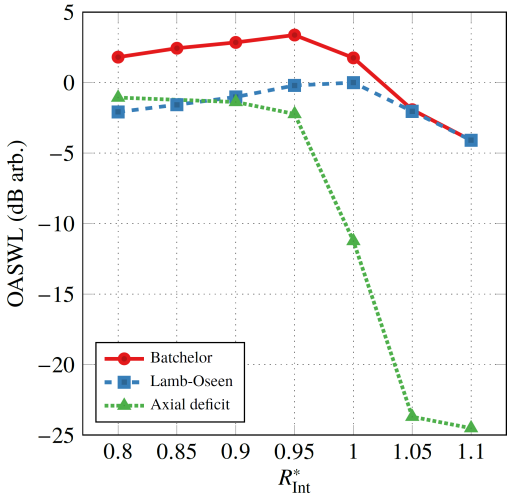

Fig. 10 Over all sound power level for different values of R^*_{Int}.

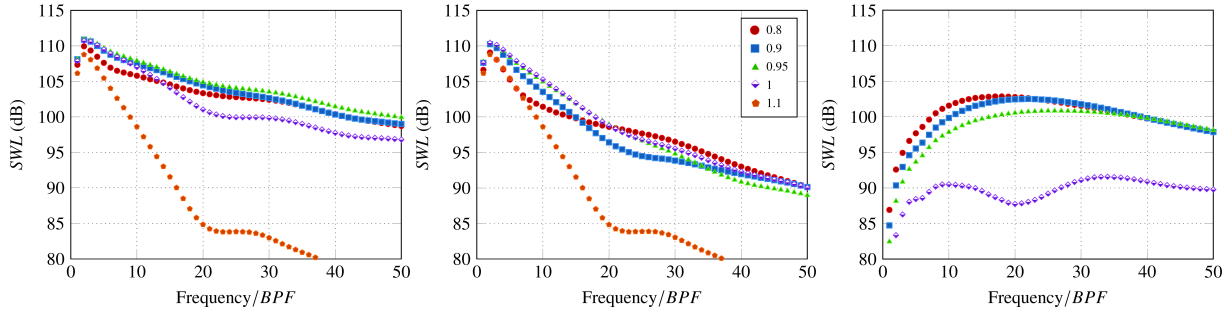

(a) Batchelor vortex. **(b) Lamb-Oseen vortex.** **(c) Axial deficit.**

Fig. 11 Radiated sound power levels depending on R^*_{Int}

For interactions with the Lamb-Oseen vortex, the frequency at which the change of slope occurs in the spectra cannot be linked to a specific component of the velocity field and appears to depend on the blade length. To investigate this point, acoustic directivities of tones below and above the transition frequency, around 10 BPF, have been plotted in Fig. 12 for the interaction at $R^*_{\text{Int}} = 0.8$. The directivity patterns are dipolar for frequencies lower than the transition frequency and quadrupolar for frequencies higher than the transition frequency. This means that the relative interaction radius act as a filter on the tangential velocity decomposition in the Fourier space. A simple analysis can be carried out based on the sketch drawn in Fig. 13. Fourier components of the vortex velocity whose wavelength are lower than twice the distance between the interaction radius and the blade tip are supported by the blade and will behave acoustically as two dipoles of opposite phase, thus leading to a quadrupolar directivity. On the contrary, Fourier components of the vortex velocity with larger wavelengths are not supported by the blade and will result only in an acoustic dipole on the blade span lower than the interaction radius. This reasoning on the transition frequency, noted f_{dq}, between dipolar and quadrupolar directivities leads to the very simple formula:

$$\frac{f_{dq}}{BPF} = \frac{\pi R^*_{\text{Int}}}{1 - R^*_{\text{Int}}} \tag{4}$$

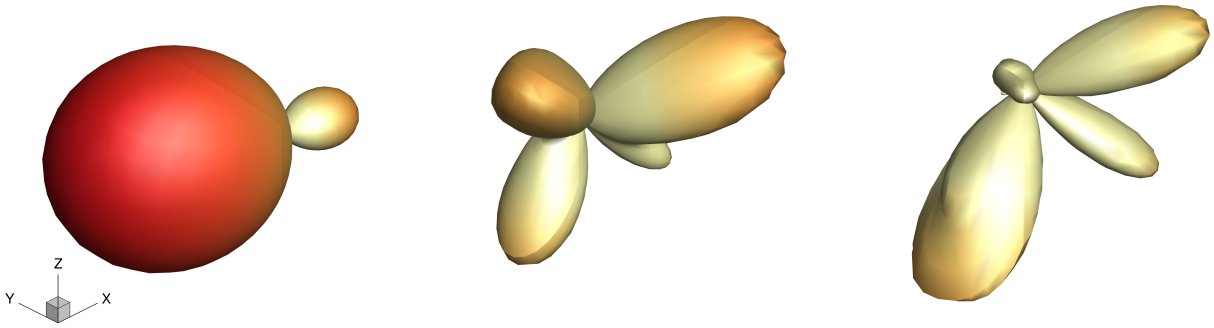

(a) $f = BPF$ **(b)** $f = 11BPF$ **(c)** $f = 21BPF$

Fig. 12 Far-field acoustic directivity of selected tones for a Lamb-Oseen vortex interaction at $R^*_{\text{Int}} = 0.8$.

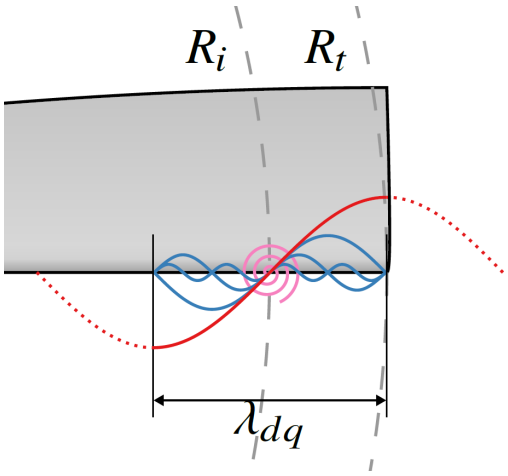

Fig. 13 Filtering of the velocity upwash by the blade.

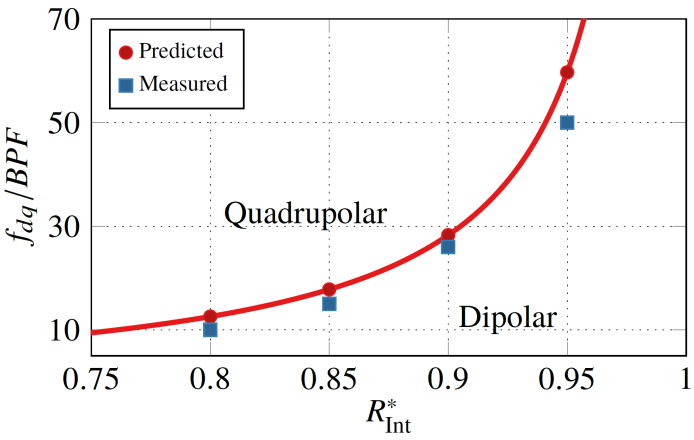

Fig. 14 Predicted and measured transition frequency between dipolar and quadrupolar directiviy patterns.

According to this formula, the transition frequency exists for any relative interaction radius in the interval $[0,1]$. This strengthens the results of Roger et al. [26] who observed a transition from quadrupolar to dipolar directivity patterns when accounting for blade span-end effect. The predicted frequency, plotted in Fig. 14, is compared to the transition frequency measured for Lamb-Oseen vortex interactions at different blade radii. Predicted values are very accurate for $R^*_{\text{Int}} \leq 0.9$ but precision diminishes as the interaction moves to the blade tip, notably due to the difficulty to identify clearly f_{dq} in the spectra.

Finally, the over all sound pressure level (OASPL) directivities are displayed in Fig. 15. For OBVI close to or above the blade tip ($R^*_{\text{Int}} \geq 0.9$), OASPL directivities exhibit a dipolar pattern for the two vortex models. For $R^*_{\text{Int}} = 0.8$, the directivity pattern of the OASPL radiated by the interaction with a Lamb-Oseen is mainly quadrupolar and this quadrupolar pattern seems partly present in the OASPL directivity of the interaction with the Batchelor vortex. Shifting the interaction radius toward the inner section of the blade would thus reduce the radiated OASWL and change the directivity into a quadrupolar pattern rather than a dipolar one.

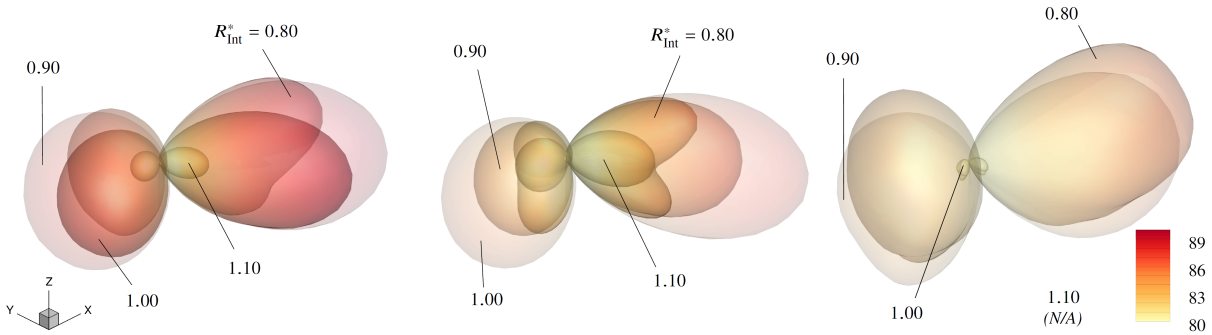

(a) Batchelor vortex. **(b) Lamb-Oseen vortex.** **(c) Axial velocity deficit.**

Fig. 15 OASPL acoustic directivity in far-field.

IV. Conclusion

The influence of vortex model and blade span on orthogonal blade/vortex interaction has been studied by means of numerical simulation relying on a validated methodology detailed in Ref. [23]. The vortex model primarily considered in this study is the Batchelor vortex, which exhibits a velocity field with tangential and axial components as do realistic tip vortices. To gain insight and deepen the analysis, simulations have also been carried out using a Lamb-Oseen vortex (azimuthal velocity only), and a purely Gaussian axial velocity deficit. Changing the vortex impingement radius on the blade is achieved by increasing or reducing the blade span and seven relative interaction radii, ranging from 0.8 to 1.1, were studied.

The main results based on the analysis of the blade aerodynamic and acoustic responses are the following: when the vortex core impinges below the blade tip, the magnitude of the thrust fluctuation and radiated noise are always higher for a Batchelor vortex than for a Lamb-Oseen vortex. For both vortex models, the thrust fluctuation and radiated noise reach their peak for an interaction close to the blade tip, exactly at the tip for a Lamb-Oseen vortex and just below (R^*_{Int} = 0.98) for the Batchelor vortex. The aerodynamic and acoustic responses decrease slowly as the vortex impingement moves inward the blade and decrease strongly as the vortex passes above the tip. Finally, the noise directivity pattern is dipolar for interaction close to or above the blade tip and becomes more and more quadrupolar as the radius of interaction moves toward the blade root. As a consequence, design optimization aiming at propeller/vortex interaction noise should not focus on sound power level only but account also for the directivity of the interaction noise.

Acknowledgments

The authors thank Yves Delrieux and Stéphanie Péron for their advises and technical support during this study.

References

[1] Woodward, R., and Gordon, E., "Noise of a Model Counterrotation Propeller With Reduced Aft Rotor Diameter at Simulated Takeoff/Approach Conditions (F7/A3)," *26th AIAA Aerospace Sciences Meeting*, 1988. doi:10.2514/6.1988-263.

[2] Coton, F. N., Marshall, J. S., Galbraith, R. A. M., and Green, R. B., "Helicopter tail rotor orthogonal blade vortex interaction," *Progress in Aerospace Sciences*, Vol. 40, No. 7, 2004-10, pp. 453–486. doi:10.1016/j.paerosci.2004.11.001.

[3] Pegg, R., and Schidler, P., "Exploratory Wind Tunnel Investigations of the Effect of Main Rotor Wake on Tail Rotor," Tech. Rep. CP-2052, NASA, 1987.

[4] Schlinker, R. H., and Amiet, R. K., "Rotor-Vortex Interaction Noise," *AIAA 8th Aeroacoustics Conference*, 1983-04-11. doi:10.2514/6.1983-720.

[5] Cary, C. M., "An Experimental Investigation of the Chopping of Helicopter Main Rotor Tip Vortices by the Tail Rotor, Part II: High Speed Photographic Study," Tech. Rep. 177457, NASA, 1987.

[6] Marshall, J. S., and Krishnamoorthy, S., "On the instantaneous cutting of a columnar vortex with non-zero axial flow," *Journal of Fluid Mechanics*, Vol. 351, 1997, pp. 41–74.

[7] Krishnamoorthy, S., and Marshall, J. S., "Three-dimensional blade–vortex interaction in the strong vortex regime," *Physics of Fluids*, Vol. 10, No. 11, 1998-11, pp. 2828–2845. doi:10.1063/1.869805.

[8] Doolan, C. J., Coton, F. N., and Galbraith, R. A. M., "Three-dimensional vortex interactions with a stationary blade," *The Aeronautical Journal*, Vol. 103, 1999, pp. 579–587.

[9] Doolan, C. J., Coton, F. N., and Galbraith, R. A. M., "Surface Pressure Measurements of the Orthogonal Vortex Interaction," *AIAA Journal*, Vol. 39, No. 1, 2001, pp. 88–95.

[10] Doolan, C. J., Coton, F. N., and Galbraith, R. A. M., "The Effect of a Preceding Blade on the Orthogonal Vortex Interaction," *Journal of the American Helicopter Society*, Vol. 46, No. 3, 2001, pp. 221–227.

[11] Howe, M. S., "On unsteady surface forces, and sound produced by the normal chopping of a rectilinear vortex," *Journal of Fluid Mechanics*, Vol. 206, 1989, pp. 131–153.

[12] Marshall, J. S., "Vortex Cutting by a Blade, Part 1: General Theory and a Simple Solution," *AIAA Journal*, Vol. 32, No. 6, 1994, pp. 1145–1150.

[13] Marshall, J. S., and Yalamanchili, R., "Vortex Cutting by a Blade, Part II: Computation of Vortex Response," *AIAA Journal*, Vol. 32, No. 7, 1994, pp. 1428–1436.

[14] Marshall, J. S., and Grant, J. R., "Penetration of a blade into a vortex core: vorticity response and unsteady blade forces," *Journal of Fluid Mechanics*, Vol. 306, 1996, pp. 83–109.

[15] Yin, J. P., and Ahmed, S. R., "Helicopter Main-Rotor/Tail-Rotor Interaction," *Journal of the American helicopter society*, Vol. 45, No. 4, 2000, pp. 293–302.

[16] Liu, X., and Marshall, J. S., "Blade penetration into a vortex core with and without axial core flow," *Journal of Fluid Mechanics*, Vol. 519, 2004, pp. 81–103.

[17] Filippone, A., and Afgan, I., "Orthogonal blade-vortex interaction on a helicopter tail rotor," *AIAA journal*, Vol. 46, No. 6, 2008, pp. 1476–1489.

[18] Saunders, D. C., and Marshall, J. S., "Vorticity reconnection during vortex cutting by a blade," *Journal of Fluid Mechanics*, Vol. 782, 2015, pp. 37–62.

[19] Saunders, D. C., and Marshall, J. S., "Transient lift force on a blade during cutting of a vortex with non-zero axial flow," *Journal of Fluid Mechanics*, Vol. 819, 2017, pp. 258—284.

[20] Falissard, F., and Delattre, G., "Investigation of Counter Rotating Open Rotor Orthogonal Blade/Vortex Interaction Noise," *20th AIAA/CEAS Aeroacoustics Conference, AIAA Aviation and Aeronautics Forum and Exposition 2014*, 2014-06-16. doi: 10.2514/6.2014-2748.

[21] Delattre, G., and Falissard, F., "Influence of Torque Ratio on Counter-Rotating Open-Rotor Interaction Noise," *AIAA Journal*, Vol. 53, No. 9, 2015, pp. 2726–2738. doi:10.2514/1.J053797.

[22] Delattre, G., Falissard, F., Vion, L., and Jacquin, L., "Open rotor interaction noise reduction through front rotor wake modification," *International Journal of Aeroacoustics*, Vol. 15, No. 1, 2016, pp. 207–227. doi:10.1177/1475472X16643461.

[23] Zehner, P., Falissard, F., and Gloerfelt, X., "Aeroacoustic study of the interaction of a rotating blade with a Batchelor vortex," *AIAA Journal*, Vol. 56, No. 2, 2018, pp. 629–647. doi:10.2514/1.J056100.

[24] Yang, Y., Zhou, T., Sciacchitano, A., Veldhuis, L. L. M., and Eitelberg, G., "Propeller and inflow vortex interaction: vortex response and impact on the propeller performance," *CEAS Aeronautical Journal*, Vol. 7, No. 3, 2016, pp. 419–428. doi: 10.1007/s13272-016-0198-z.

[25] Yang, Y., Veldhuis, L. L. M., and Eitelberg, G., "Aerodynamic impact of a streamwise vortex on a propeller," *Aerospace Science and Technology*, 2017. doi:10.1016/j.ast.2017.08.004.

[26] Roger, M., Schram, C., and Moreau, S., "On vortex-airfoil interaction noise including span-end effects, with application to open-rotor aeroacoustics," *Journal of Sound and Vibration*, Vol. 333, No. 1, 2014, pp. 283–306. doi:10.1016/j.jsv.2013.09.012.

[27] Quaglia, M. E., Léonard, T., Moreau, S., and Roger, M., "A 3D analytical model for orthogonal blade-vortex interaction noise," *Journal of Sound and Vibration*, Vol. 399, 2017, pp. 104–123. doi:10.1016/j.jsv.2017.03.023.

[28] Moreau, S., and Roger, M., "Advanced noise modeling for future propulsion systems," *International Journal of Aeroacoustics*, Vol. 17, No. 6-8, 2018, pp. 576–599.

[29] Zehner, P., Falissard, F., Péron, S., and Gloerfelt, X., "Influence of Blade Thickness and Blade Span on Orthogonal Blade/Vortex Interaction Noise," *23rd AIAA/CEAS Aeroacoustics Conference*, 2017. doi:10.2514/6.2017-3531.

[30] Falissard, F., Lerat, A., and Sidès, J., "Computation of Airfoil Vortex Interaction Using a Vorticity-Preserving Scheme," *AIAA Journal*, Vol. 46, No. 7, 2008, pp. 1614–1623.

[31] Batchelor, G. K., "Axial flow in trailing line vortices," *Journal of Fluid Mechanics*, Vol. 20, No. 4, 1964, pp. 645–658. doi:10.1017/S0022112064001446.

[32] Oseen, C. W., "Über Wirbelbewegung in einer reibenden Flüssigkeit," *Arkiv för matematik, astronomi och fysik*, Vol. 7, 1911, pp. 1–13.

[33] Lamb, H., *Hydrodynamics*, Sixth edition, chap. XI, §334-a. Cambridge University Press, 1932.

[34] Péron, S., and Benoit, C., "Automatic off-body overset adaptive Cartesian mesh method based on an octree approach," *Journal of Computational Physics*, Vol. 232, No. 1, 2013, pp. 153–173. doi:10.1016/j.jcp.2012.07.029.

[35] Benoit, C., Péron, S., and Landier, S., "Cassiopee: a CFD pre- and post-processing tool," *Aerospace Science and Technology*, Vol. 45, 2015-09, pp. 272–283. doi:10.1016/j.ast.2015.05.023.

[36] Saunier, O., Benoit, C., Jeanfaivre, G., and Lerat, A., "Third-order Cartesian overset mesh adaptation method for solving steady compressible flows," *International Journal for Numerical Methods in Fluids*, Vol. 57, No. 7, 2008-07-10, pp. 811–838. doi:10.1002/fld.1646.

[37] Saunier, O., Péron, S., Jeanfaivre, G., Benoit, C., and Lerat, A., "High-order accurate Cartesian partitioning methods. Application to rotor flows," *33rd ERF, European Rotorcraft Forum*, 2007-09-13, pp. 1–16. doi:20.500.11881/216.

[38] Ffowcs Williams, J. E., and Hawkings, D. L., "Sound Generation by Turbulence and Surfaces in Arbitrary Motion," *Philosophical Transactions of the Royal Society*, Vol. 264, 1969, pp. 321–342. doi:10.1098/rsta.1969.0031.

[39] Prieur, J., and Rahier, G., "Aeroacoustic integral methods, formulation and efficient numerical implementation," *Aerospace Science and Technology*, Vol. 5, No. 7, 2001, pp. 457–468. doi:10.1016/S1270-9638(01)01123-3.

[40] Nelson, W. C., *Airplane propeller principles*, John Wiley & Sons, 1944.